SCIENTIFIC REPORTS
nature research

Check for updates

OPEN

Divalent heavy metals and uranyl cations incorporated in calcite change its dissolution process

Xiaohang Zhang[1,2], Jianan Guo[1,2], Shijun Wu[1]✉, Fanrong Chen[1] & Yongqiang Yang[1]

Due to the high capacity of impurities in its structure, calcite is regarded as one of the most attractive minerals to trap heavy metals (HMs) and radionuclides via substitution during coprecipitation/crystal growth. As a high-reactivity mineral, calcite may release HMs via dissolution. However, the influence of the incorporated HMs and radionuclides in calcite on its dissolution is unclear. Herein, we reported the dissolution behavior of the synthesized calcite incorporated with cadmium (Cd), cobalt (Co), nickel (Ni), zinc (Zn), and uranium (U). Our findings indicated that the HMs and U in calcite could significantly change the dissolution process of calcite. The results demonstrated that the incorporated HMs and U had both inhibiting and enhancing effects on the solubility of calcite, depending on the type of metals and their content. Furthermore, secondary minerals such as smithsonite ($ZnCO_3$), Co-poor aragonite, and U-rich calcite precipitated during dissolution. Thus, the incorporation of metals into calcite can control the behavior of HMs/uranium, calcite, and even carbon dioxide.

Calcite, the most stable polymorph of $CaCO_3$, is the most important and also the most abundant carbonate mineral on Earth[1–3]. The precipitation of calcite serves as a sink of metals[4–7], organic material[8], and carbon dioxide[9,10]. Traditionally, lime materials (including calcite, burnt lime, and dolomite) are used to neutralize acidic soils and to overcome the problems associated with soil acidification[11,12]. With the application of calcite, heavy metals (HMs) usually become less bioavailable due to the increase in soil pH and formation of metal–carbonate bounded complexes[13,14]. Furthermore, in situ microbial induced calcite precipitation (MICP) was proposed to remediate soil and underground water contaminated by HMs or radionuclides via substitution/coprecipitation[15,16]. Nevertheless, as much as 30% calcite dissolution was observed, which challenges the long-term sustainability of the calcite formed by MICP[17].

As a base mineral, the dissolution of calcite can neutralize the acidification of soil and water. During the last two centuries, acidification of Earth's air, water, and soil has been accelerated due to anthropogenic activities, such as the combustion of fossil fuels and smelting of ores, mining of coal and metal ores, and application of nitrogen fertilizer to soils[18,19]. Due to ocean acidification[20], the dissolution of marine $CaCO_3$ (including sediments and coral reef) has been reported worldwide[21–24]. On the continent, the concentrations of Ca in freshwater increased due to terrestrial rock dissolution as a result of climate change and anthropogenic acid deposition[25,26]. Meanwhile, the carbonate bonded metal will release into the environment, which could make calcite a potential source of heavy metals[27,28]. For example, uranium concentrations in river water are primarily determined by the dissolution of limestone (dominated by calcite)[29]. Strontium (Sr) released from Himalayan carbonate changed the Sr isotope composition in seawater and marine limestones[30]. In the Karst area, the weathering of carbonate rock naturally causes HMs to accumulate in soil[31–34], resulting in HM pollution in plants[35].

The growth and dissolution of calcite have been investigated extensively and reviewed in documents[36–38]. Generally speaking, the dissolution of calcite is influenced by the temperature, pH, P_{CO_2}, solution composition and inhibitors[36–39]. However, the influence of impurities in calcite on its dissolution is not well understood. Based on atomic force microscopy (AFM) observations, Harstad and Stipp concluded that Fe^{2+}, Mg^{2+}, Mn^{2+}, and Sr^{2+}, which are naturally present in Iceland spar calcites, inhibited the dissolution of calcite[40]. However, at least for Mg^{2+} and Mn^{2+}, this conclusion conflicts with the experimental data obtained from magnesian calcite[41–44] and synthesized Mn^{2+} containing calcite[45]. The macroscopic dissolution experiment of natural inorganic, biogenic,

[1]CAS Key Laboratory of Mineralogy and Metallogeny/Guangdong Provincial Key Laboratory of Mineral Physics and Materials, Guangzhou Institute of Geochemistry, Chinese Academy of Sciences, 511 Kehua Street, Guangzhou 510640, China. [2]University of Chinese Academy of Science, 19 Yuquan Road, Beijing 100049, China. ✉email: wus@gig.ac.cn

Sample	Mineral composition	M^{2+}/Ca^{2+} (mol%)		BET specific surface area (m^2/g)
		Added	Measured	
M0	Cal*	–	–	0.17
Cd-02	Cal	2.00	1.83	0.38
Cd-04	Cal	4.00	4.05	0.57
Cd-06	Cal	6.00	6.75	1.02
Cd-08	Cal	8.00	9.31	1.57
Cd-10	Cal	10.00	11.73	1.66
Zn-02	Cal	2.00	1.89	0.43
Zn-04	Cal	4.00	3.18	1.65
Zn-06	Cal	6.00	4.83	1.69
Zn-08	Cal	8.00	7.04	2.93
Zn-10	Cal	10.00	12.36	4.49
Co-02	Cal	2.00	1.37	0.25
Co-04	Cal	4.00	3.43	0.53
Co-06	Cal	6.00	6.40	0.80
Co-08	Cal	8.00	7.72	1.39
Co-10	Cal, arg*	10.00	–	–
Ni-0.04	Cal	0.04	0.05	0.19
Ni-0.08	Cal	0.08	0.07	0.21
Ni-0.2	Cal	0.20	0.28	0.22
Ni-0.4	Cal, vat, arg	0.40	–	–
U-0.5	Cal	0.50	0.56	0.51
U-01	Cal	1.00	0.95	0.69
U-02	Cal	2.00	1.55	1.46
U-04	Cal	4.00	2.64	4.64
U-08	Cal, vat*	8.00	–	–

Table 1. Mineral/chemical compositions and BET specific surface areas of the synthesized samples. *Cal, vat, and arg are abbreviations for calcite, vaterite, and aragonite, respectively.

and synthesized samples demonstrated that the dissolution ability of magnesian calcite is positively correlated with the content of Mg in calcite[41–43], which is supported by the AFM observation, according to Davis and his coauthors[44]. Therefore, high-Mg calcite in tropical continental shelf sediments is more sensitive than low-Mg calcite to ocean acidification[46]. Recently, we found that the incorporation of Cu^{2+} and Mn^{2+} enhanced the solubility of calcite[45]. The above-mentioned studies indicated that the influences of impurities on calcite dissolution is complex and need further investigation.

Because of the multiformity of heavy metal contamination in the field and the numerous impurities in natural calcite, it is difficult to identify the influence of a single component on its dissolution. Herein, we provide further evidence on the dissolution behavior of synthesized calcite incorporated with Cd^{2+}, Co^{2+}, Ni^{2+}, Zn^{2+} and UO_2^{2+}, which are common environmental pollutants. The results showed that the solubility of calcite was inhibited by coprecipitated Cd^{2+} and Ni^{2+} but enhanced by Co^{2+}. Unexpectedly, Zn^{2+} and UO_2^{2+} showed both inhibiting and enhancing effects, depending on the mass of the impurities in calcite. These observations suggested that the incorporated HMs and radionuclides might control the dissolution of calcite. Inversely, the migration of HMs and radionuclides could be remarkably controlled by the host minerals as well.

Results

Characterization of calcite incorporated with impurity metals. With the addition of HMs, the XRD patterns of all the Cd and Zn containing products were the same as the pure calcite reference pattern, indicating that no detectable secondary crystalline phases were present (Fig. S1a,b, Table 1). However, traces of aragonite were found in sample Co-10 (Fig. S1c), while vaterite was present in U-08 and U-10 (Fig. S1e). Meanwhile, both aragonite and vaterite occurred in Ni-0.4 and Ni-01 (Fig. S1d). To avoid the impact of aragonite and vaterite, we used samples without detectable secondary phases for further experiments.

As shown in Fig. 1a, pure calcite showed a typical rhombohedral morphology as a euhedral calcite crystal. With the incorporation of metals, the morphology changed to aggregates of semi-euhedral or anhedral (dumbbell) phases with small sizes (Fig. 1b–l). This trend is supported by the BET surface area data, which are positively correlated with the molar fraction of metals, with R^2 values of 0.65 (Ni), 0.89 (Co), 0.93 (U), and 0.96 (Cd, Zn) (Table 1, Fig. S2). Usually, the incorporation of impurities will decrease the sizes of crystals[47,48] due to the inhibition of the crystal growth.

Figure S3 showed the spatial distribution of metals in typical polished HM-calcite. Both of the line scan and elemental mapping results showed the presence of Cd/Zn-rich cores in Cd/Zn-calcite (Fig. S3a–h). However, the

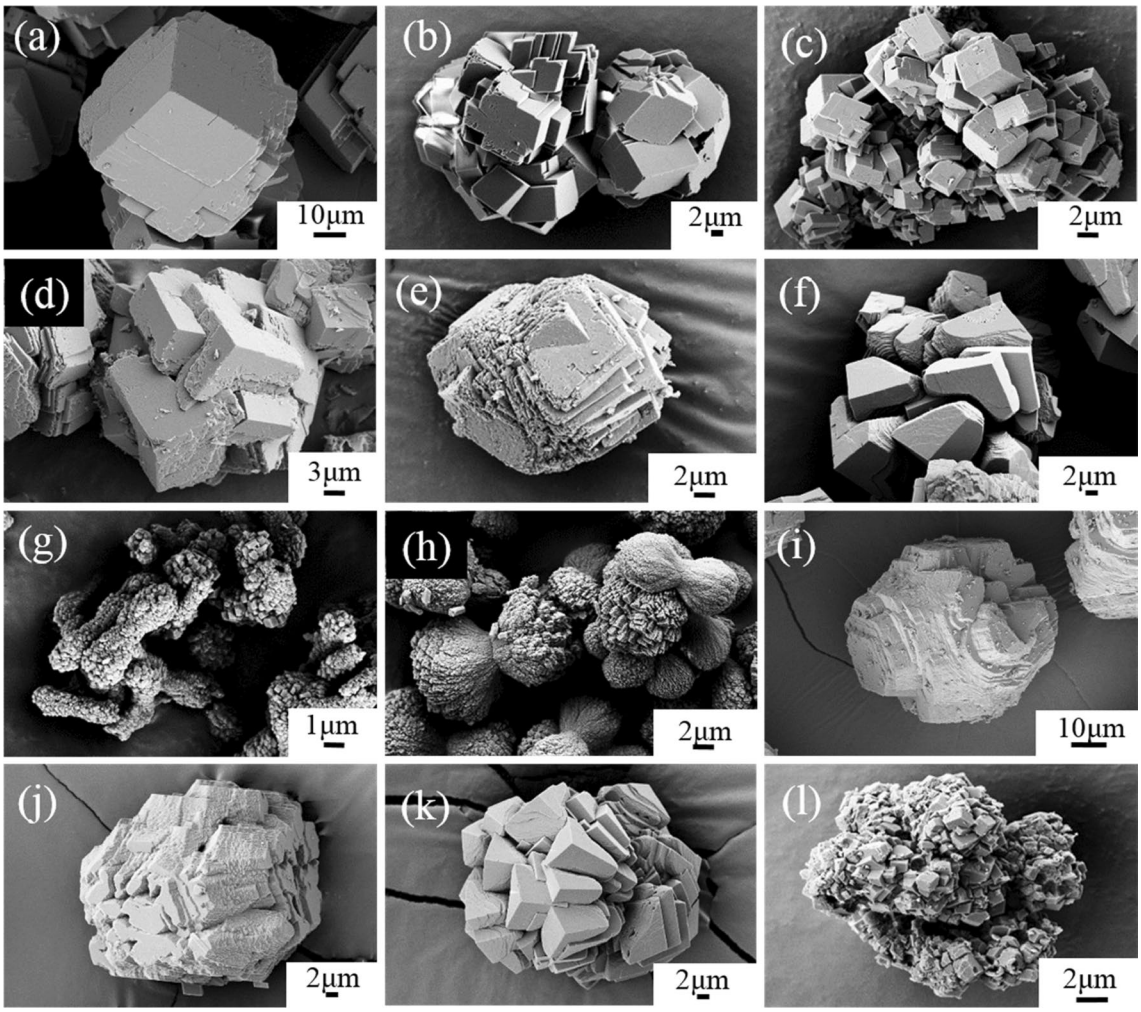

Figure 1. SEM images of selected calcite. (**a**) M0, (**b**) Cd-02, (**c**) Cd-10, (**d**) Zn-02, (**e**) Zn-10, (**f**) Co-02, (**g**) Co-06, (**h**) Co-08, (**i**) Ni-0.04, (**j**) Ni-0.2, (**k**) U-0.5, and (**l**) U-04.

Co-calcite and Ni-calcite were quite homogenous in general. Interestingly, U-calcite possessed two distributions, as mentioned above, i.e., a U-rich core and homogenous distribution.

Release of metals during the dissolution of calcite. Once calcite contacted the solution, dissolution occurred immediately, especially in an acidic solution. For example, when the initial solution pH ranged from 1.0 to 8.9, the proportion of pure calcite that dissolved within 20 min accounted for 83.8–97.4% of the total mass dissolved within 120 min (Fig. S4). However, the dissolution process proceeded until equilibrium was reached at approximately 2400 h with an initial pH of 5.0. (Fig. 2). The total dissolved calcium and solution pH at equilibrium for pure calcite were 0.52 mM and 8.19 (Figs. 2, S5), respectively, which are both very close to the theoretical data (0.53 mM and 8.22) in an open system. There was 5 mL of air in each of the closed tubes in our experiment, resulting in a semi-open system. Since the annual global average carbon dioxide (CO_2) concentration on Earth's surface was 407.4 ± 0.1 mg L^{-1} in the year 2018[49], the closed CO_2 in each tube was no less than 0.046 mmol, which can dissolve into the alkaline solution. However, this tiny CO_2 amount was not enough to increase the DIC up to 1.03 mmol at equilibrium. Therefore, the effect of environmental CO_2 on the experiment was not significant.

With the incorporation of HMs and uranium, the quantity of dissolved calcium changed, even at the early stage (first two hours) of dissolution (Table S2). After two hours of dissolution, the dissolved Ca concentrations were 0.13–0.15 mM and 0.15–0.07 mM for all the Cd- and Ni-incorporated calcite (Cd/Ni-calcite), which were less than the dissolved Ca concentration in the control (0.16 mM) (Fig. 2a,g and Table S2). On the contrary, more Ca was dissolved in Zn-calcite than in Cd/Ni-calcite (0.18–0.23 mM) (Fig. 2c and Table S2). However, Co and U showed inhibition effects at low contents (0.14 and 0.15 mM for Co-2 and U-0.5) and an enhancement at a high content (0.17–0.22 mM for Co-06/08 and 0.16–0.31 mM for U-01/02/04) (Fig. 2e,i and Table S2). When calibrated with the BET surface area, the dissolution rates within the first 2 h for all heavy metal-incorporated calcites (2.90–31.70 μmol/m^2·h) were less than those for the pure calcite (37.36 μmol/m^2·h) (Fig. S6). This suggested that the dissolution rate was controlled both by the mineral surface area and the fraction of HMs. After 2880 h,

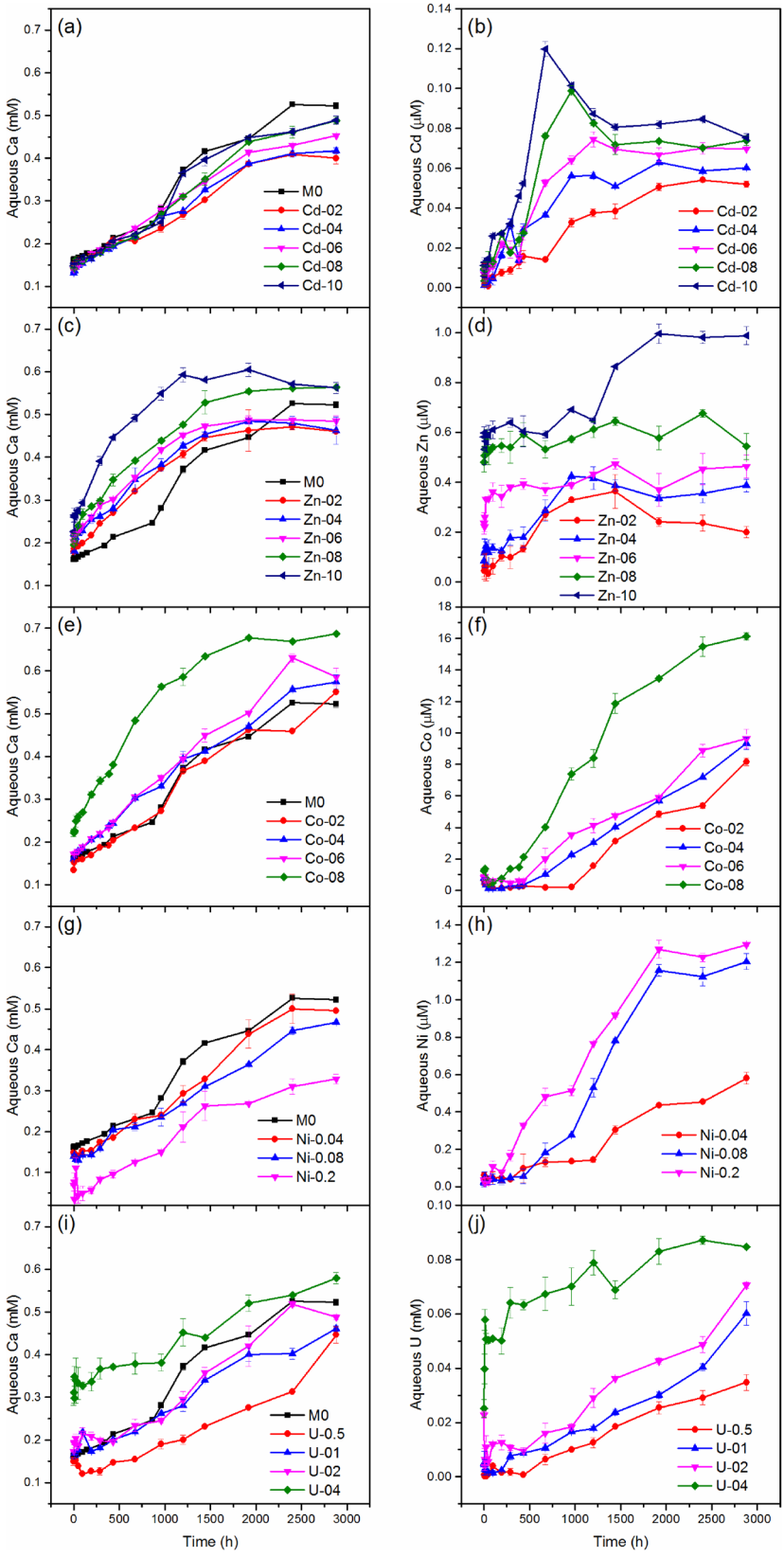

Figure 2. Evolution of the aqueous metal concentration during the dissolution of calcite. Left panels, the concentration of dissolved Ca^{2+}. Right panels, the concentration of dissolved HMs, and uranium.

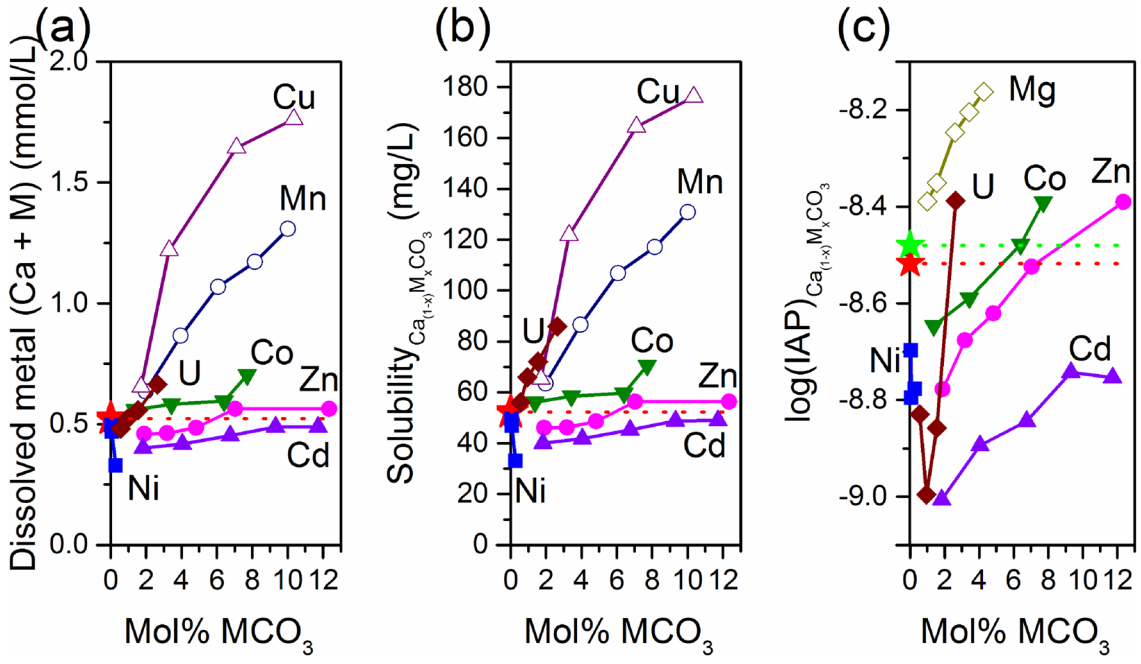

Figure 3. The concentration of total dissolved metals, the calculated solubility, and log(IAP) varied with the content of HMs. The red and green star/dashed lines indicate the result of the pure calcite obtained in this investigation and from the Minteq(V4) database in Phreeqc. IAP $= \alpha_{Ca^{2+}} \bullet \alpha_{CO_3^{2-}}$. The data of Cu and Mn were taken from Zhang et al.[45], and the data of Mg were obtained from Davis et al.[44].

less Ca dissolved for Cd-calcite (0.40–0.49 mM) and Ni-calcite (0.50–0.33 mM) than for pure calcite (0.52 mM) (Fig. 2a,g), while more Ca dissolved for Co-calcite (0.55–0.69 mM) (Fig. 2e) than for pure calcite. Surprisingly, Zn and U showed both inhibition (0.46–0.48 mM for Zn-02/04/06 and 0.45–0.49 mM for U-0.5/01/02) and enhancement effects (0.56 mM for Zn-08/10 and 0.58 mM for U-04), depending on the proportion of impurities in calcite (Fig. 2c,i).

As expected, all the HMs and uranium released into the solution together with calcium, and the amounts released increased with time until reaching equilibrium, excepted for Co-calcite, Ni-0.04, and U-0.5/01/02, which did not reach equilibrium, even after 2880 h (Fig. 2f,h,j). Note that Cd-08 and Cd-10 displayed peak values of Cd at 960 h and 672 h (Fig. 2b), which is similar to the phenomenon observed for Cu-calcite and Mn-calcite[45]. The final released HM concentrations were 0.05–0.08 μM for Cd (Fig. 2b), 0.20–0.99 μM for Zn (Fig. 2d), 8.15–16.13 μM for Co (Fig. 2f), 0.58–1.29 μM for Ni (Fig. 2h) and 34.78–84.76 μM for U (Fig. 2j). The proportions of released Cd, Zn, Co, Ni and U were 0.01–0.02‰, 0.06–0.09‰, 1.11–4.03‰, 0.31–1.22‰ and 3.29–9.96% of the total loaded metals, respectively.

As demonstrated in Fig. S7, the molar ratios of total dissolved metals were 0.09–0.18‰ for Cd/Ca, 0.43–1.75‰ for Zn/Ca and 1.48–2.35% for Co/Ca, which were much less than those in the solids, except for Co-02, suggesting the nonstoichiometric release of Cd, Zn, Co and Ca. Contrarily, the molar ratios of released Ni/Ca and U/Ca were 1.17–3.93‰ and 7.23–14.63%, which are both higher than those in the solids (0.5–2.8‰ and 0.56–2.64%). These data demonstrated that all the studied HMs and U showed nonstoichiometric release behaviors during the dissolution of calcite. In particular, Ni and U tend to passively release into the solution, while Cd, Zn, and Co prefer to prevent dissolution.

Figure 3 showed the total dissolved metals (Ca + M) and the corresponding solubility at 2880 h. Since the content of impurities is low in calcite, the addition of released HMs did not change the relationship between the total dissolved metals and the content of impurities (Fig. 3a). The calculated solubility was 52.26 mg/L for pure calcite, 40.03–48.90 mg/L for Cd-calcite, and 49.59–32.99 mg/L for Ni-calcite, showing the inhibition of calcite dissolution with the incorporation of Cd and Ni. Comparably, the solubility of Co-calcite and U-calcite enhanced to 56.05–70.62 mg/L and 56.13–85.90 mg/L, respectively. Meanwhile, the solubility of Zn-calcite showed both inhibition (46.05–48.54 mg/L for Zn-02/04/06) and enhancement (56.41–56.37 mg/L for Zn-08/10) (Fig. 3b). As is known, the solubility of a material at equilibrium is independent of its surface area. Therefore, the relationship between the solubility of calcite and the molar fraction of HMs was fitted using linear equations, which provided an R^2 value of 0.96, 0.79, 0.69, 0.99 and 0.98 for Cd, Zn, Co, Ni, and U, respectively (Table S3). Except for Ni, the solubility of calcite is positively correlated with the molar fractions of HMs, which are the same as those of Mg-calcite[41–44], Cu-calcite, and Mn-calcite[45].

K_{sp} and IAP are generally used to characterize the solubility of a material and are calculated using the ion concentration or activity. As shown in Fig. 3c, the data of all the IAP values were calculated using the ion activity of Ca^{2+} and CO_3^{2-} according to Eq. (8). In addition to U, the graphs of Cd, Zn, Co, and Ni showed a tendency similar to that shown in Fig. 3a and b. When we tried to calculate the IAP using Eq. (9), we obtained results

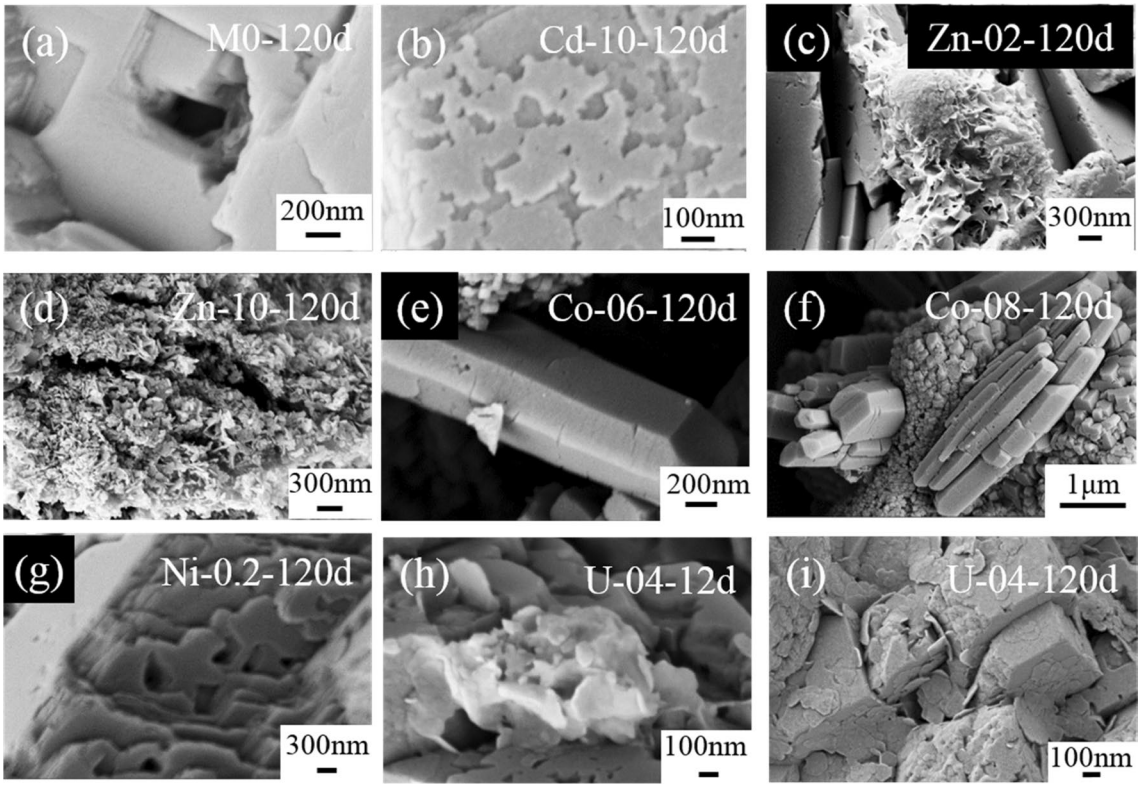

Figure 4. SEM images of selected calcite after dissolution. Sample names on the top-right of each figure were labeled as sample name-T, e.g., Cd-10-120d stands for Cd-10 after 120 days of dissolution.

	Secondary minerals			Calcite before dissolution
Sample	Ca%	M%	(M/Ca)%	(M/Ca)%
Zn-10	0.08	22.14	27.675	12.36
Co-08	23.82	0.22	0.92	7.72
U-04	4.09	1.17	28.61	2.64

Table 2. Chemical molar compositions of the secondary minerals obtained by TEM-EDS.

similar to those shown in Fig. 3c. Since the ion activity cannot be measured directly, we recommend using the total concentration of metals to express the solubility of impure calcite. This method should be more convenient in the field.

Morphology change and precipitation of secondary minerals during the dissolution of calcite. After dissolution, typical etch pits were present on the surfaces of pure calcite (Figs. 4a, S8a–f) and Cd/Ni-calcite (Figs. 4b,g, S8g–l). Unexpectedly, some secondary minerals precipitated on the surface of Zn/Co/U-calcite (Figs. 4c–f,h,i, S9, S10). These secondary minerals were composed of lamelliform nanocrystals for Zn/U-calcite and prism nanocrystals for Co-calcite. Meanwhile, the secondary minerals formed earlier in the samples with a high content of impurities than in the one with a low content, i.e., new precipitates were first observed after 12 and 28 days for U-04 and U-02, respectively. As shown in Table 2 and Fig. S11, the EDS data demonstrated that the secondary minerals of Zn-10 and U-04 were rich in Zn and U, while Co-08 contained trace Co, which was distinguished with the calcite before dissolution.

Furthermore, high resolution transmission electron microscopy (HRTEM) and selected area electron diffraction (SAED) were used to characterize the secondary minerals (Fig. 5). The HRTEM image of the secondary minerals of Zn-10 (Fig. 5a) revealed the lattice fringes of the smithsonite ($ZnCO_3$) (104) plane (d = 2.77 Å) and (116) plane (d = 1.72 Å) (RRUFF[50]), which was further validated by the SAED patterns (Fig. 5b). This observation agreed with the content of Zn being much higher than that of Ca, according to the EDS data. For the secondary mineral of Co-08, the HRTEM images show lattice spacings of 2.73 Å and 2.48 Å (Fig. 5c,e), which can be indexed to the (121) and (200) planes of aragonite (RRUFF[51]). The relative SAED patterns (Fig. 5d,f) further proved that they are single crystals of aragonite along the [311] and [020] directions. Moreover, the elongated prismatic morphology supported the occurrence of aragonite (Figs. 4e,f, S10c–h). Furthermore, the Raman

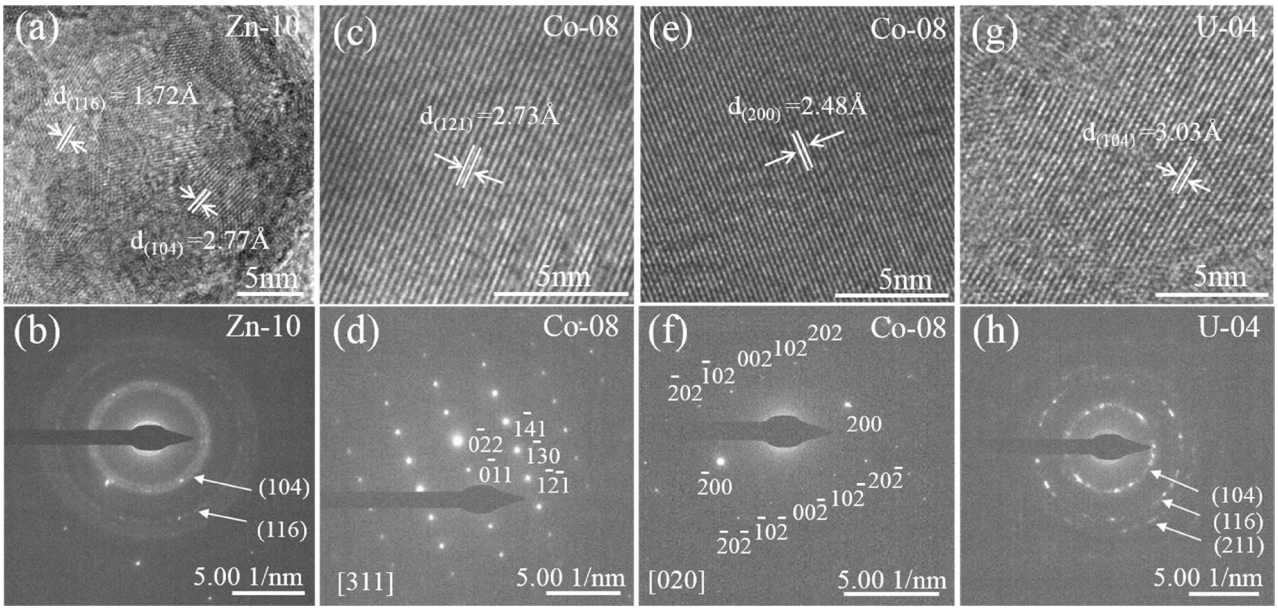

Figure 5. HRTEM images and SAED patterns of selected secondary minerals.

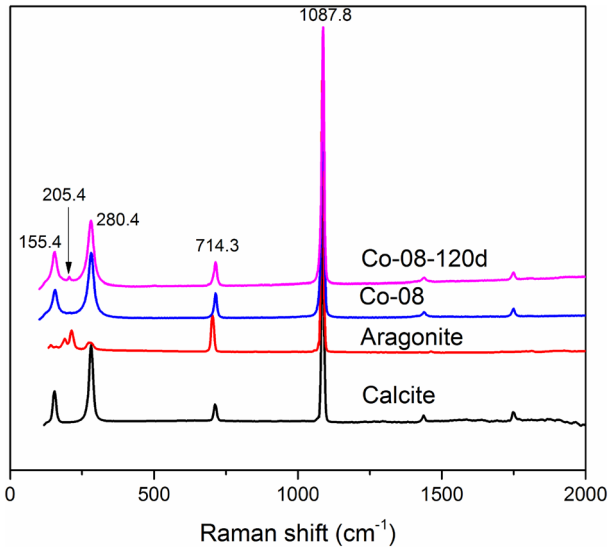

Figure 6. Raman spectra of the secondary mineral of Co-08.

peak at 205.4 cm^{-1} confirmed that aragonite was a secondary mineral in Co-08-120d (Fig. 6). Comparably, the HRTEM images of the secondary minerals of U-04 possessed lattice fringes with a d-spacing of 3.03 Å, which corresponded to the (104) reflection of calcite (RRUFF[52]) (Fig. 5g), as confirmed by the SEAD pattern (Fig. 5h). Therefore, the secondary minerals observed in our experiment were Ca-poor smithsonite, U-rich calcite, and Co-poor aragonite.

Discussion

The incorporation of impurities in calcite. Divalent cations, particularly those with an ionic radius close to that of Ca^{2+}, easily substitute for Ca^{2+} in the structure of calcite[53]. The experiments and simulation well demonstrated the incorporation of Cd^{2+}[54–62], Co^{2+}[55,57,62–68], Zn^{2+}[58,62,64,65,69–75], Ni^{2+}[76–79] and UO_2^{2+}[80–91] into the structure of calcite. In this study, the presence of aragonite and vaterite indicated the favoritism of these phases in the high concentration Co, Ni, and U system. The incorporated Co, Ni, and U in $CaCO_3$ could stabilize aragonite or vaterite phases, agreeing well with previous investigation[66,83]. Taking U as an example, a previous study reported that the U concentration in synthesized aragonite was higher than that in calcite, even though both of them grew in a solution containing the same concentration of uranium[90]. This phenomenon could be attributed

to the thermodynamic preference of U incorporation into aragonite[92]. Another reason was that aragonite has a higher surface area than calcite and can absorb more U on its surface. Aragonite was present only in Co-10, even though equal stoichiometric amounts of HMs were used for the synthesis of Cd-10, Zn-10, and Co-10. The exception of Co-10 demonstrated that the tolerance of the calcite structure for the impurity metals would be varied with its ionic radii, following the Goldschmidt's Rules.

Traditionally, it is believed that the incorporated divalent cations would take the crystallographic site of Ca^{2+}[53]. However, it is difficult to determine the coordination environment and, thus, the incorporation modes of the impurities until the development of extended X-ray absorption fine structure spectroscopy (EXAFS). According to the experimental EXAFS data and Ab initio molecular dynamics simulation, there are at least five models of incorporating impurities in calcite. (1) Isovalent substitution occurs for Ca^{2+} with sixfold coordination, which is the same as the coordination of Ca^{2+} in calcite, e.g., Ba^{2+}, Cd^{2+}, Co^{2+}, Mn^{2+}, Pb^{2+}, Sr^{2+} and Zn^{2+}[64,65,69,93–95]. (2) Aliovalent substitution occurs for Ca^{2+} with six-fold coordination, e.g., Nd^{3+}, Sm^{3+}[96], Np^{5+}[97], U^{4+}[98] and U^{6+} (as UO_2^{2+}) in natural calcite[84,87]. (3) Aliovalent substitution occurs for Ca^{2+} with seven-fold coordination, e.g., Dy^{3+}, Yb^{3+}[96], Am^{3+}[99] and U^{6+} (as UO_2^{2+}) in synthesized calcite[80,81]. (4) Impurities can occupy the CO_3^{2-} site, e.g., IO_3^-[100,101] CrO_4^{2-}, SeO_3^{2-}, AsO_3^{3-}[101–104] and AsO_4^{3-}[105]. (5) As the second phase or nanophase impurity, e.g., Ba occurs dominantly as $BaSO_4$ in natural Ba-rich calcite[64], nano hydrozincite ($Zn_5(CO_3)_2(OH)_6$) and sphalerite (ZnS) discovered in foraminiferal calcite shells[69]. Furthermore, the incorporation of monovalent cations, i.e., Na^+ and Li^+, might be required to achieve a local charge balance in the calcite lattice[98,106]. In Zn-contaminated foraminiferal calcite shells, adsorption, isovalent substitution, and second nanophases coexisted with each other[69]. Coexisting multimechanisms are probably much more common in the natural system and high concentrations of impurities than in the other systems.

The spatial distribution of trace elements in biogenic calcite might be homogeneous or heterogeneous, which relates to the temperature, growth rate, or organic matter content[69,107–110]. Due to the overgrowth of crystals, the heterogeneous distribution of impurities has been discovered in natural single crystals of low-temperature precipitated calcite[7,111]. In laboratory-synthesized calcite, the distribution of trace elements is not reported very often, even though heterogeneous distribution sometimes occurrs[66,112]. However, the HM-calcites in our experiment showed both heterogeneous (Cd, Zn, U) and homogeneous (Co, Ni, U) distributions. The homogeneous distribution of Co in Co-08 differed from the result of Katsikopoulos et al.[66], probably due to the visible difference in the Co fractions in the solid phases, i.e., a Co/Ca molar ratio of 0.077 in Co-08 versus 1.67 in the previously published data. Unexpectedly, some U-04 particles showed heterogeneous distributions of uranium, while other particles showed homogeneous distributions. This phenomenon indicated the complexity of the distribution of impurities in HM-calcite, which required further investigations.

The influence of incorporated impurities on the dissolution of calcite. Since the natural water chemistry, e.g., seawater chemistry, is complex, numerous investigations have demonstrated that the dissolution of calcite is affected by the water constituents, including the major, minor, and trace constituents, regardless of whether the constituents are inorganic or organic[36–38]. Based on the inhibition dissolution of natural calcite, e.g., limestone and marble, Svensson and Dreybrodt suggested that Ca^{2+} ions are adsorbed to impurities at the surface of the natural mineral to form a complex, which acts as an inhibitor[113]. Subsequently, Eisenlohr et al. suggested that aluminosilicate nano-complexes could incorporate in the calcite matrix. During dissolution, these impurities will release from the calcite matrix and then will be adsorbed irreversibly at the reacting surface, where they act as inhibitors[114].

Except for Mg^{2+}, the influence of the impurities incorporated metals in solids on the dissolution of calcite is unknown. According to the dissolution of magnesian calcite, the Mg^{2+} in calcite enhanced the mineral solubility through magnesium incorporation and inhibited calcite growth[41–44]. On the one hand, high magnesian calcite compositions exist within the spinodal gap and are therefore unstable. On the other hand, calcite growth is inhibited through either step-blocking by Mg^{2+} adsorption and slow dehydration or enhanced the mineral solubility associated with Mg^{2+} incorporation[41–44]. Contrarily, Harstad and Stipp reported that naturally present trace metals (Fe^{2+}, Mg^{2+}, Mn^{2+}, and Sr^{2+}) inhibited the dissolution rate of calcite based on AFM observations[40]. Recently, we demonstrated the enhanced dissolution of calcite once Cu^{2+} and Mn^{2+}[45] were incorporated. These results contradicted each other with regards to the role of Mg^{2+} and Mn^{2+} play in calcite dissolution.

Firstly, the calcite used by Harstad and Stipp contained many impurity metals. Therefore, the enhancement effect contributed by Mg^{2+} and Mn^{2+} might be neutralized by other inhibitors, such as Fe^{2+} and Sr^{2+}. Secondly, the relationship between the impurity molar fractions was inconsistent with the solubility/dissolution rate, as shown in Figs. 3 and S6. It has been observed that the surface area-normalized dissolution rates increase non-linearly with decreasing the initial crystal size[115]. However, the normalized dissolution rates of our impurity-containing calcite with small crystal sizes were lower than that of the large pure calcite, suggesting the inhibition of the dissolution rate by the impurities. This inconsistency indicates that the impurity-containing calcite required a longer time than pure calcite to reach equilibrium, as described previously. According to Fig. 2, the pure calcite reached equilibrium at approximately 2880 h, while Cd-calcite, Ni-calcite, and U-calcite still have an upward trend, suggesting that Cd/Ni/U-calcite did not reach equilibrium at that time. Third, the dissolution rate obtained from reactor experiments performed on crushed crystals (i.e., mineral powders) differed from that measured locally at the surface of polished or pristine crystals[116]. This phenomenon is ascribed to the differences in the surface reactivity distribution at the two scales of observation and different sample preparation methods, which could change the distribution of reactive sites[116]. In our samples, the BET surface area increased with the increase in the molar fraction of impurities, which partially due to the small crystal size. Compared to large crystals, the crystals with small sizes will provide more crystal edges, which can control the dissolution at the crystal scale. However, the contribution of the edges to the overall dissolution is crystal-size- and

time-dependent, which is not well understood yet[116]. Furthermore, one should be very careful to hand these phenomena since the surface area-normalized dissolution rates increase non-linearly with decreasing initial crystal sizes[115]. Last but not least, the heterogeneous distribution of impurities in Cd/Zn/U-calcite should contribute more or less to the nonstoichiometric release of Cd, Zn, and U. We propose that the nonstoichiometric release of Cd, Zn during the weathering of Cd/Zn-bearing limestone is one of the reasons that Cd and Zn enrich the soil in the Karst area[31–34,117].

The precipitation of secondary minerals during the dissolution of calcite. In principle, the chemical weathering of rocks involves the coupled dissolution of the primary minerals and precipitation of more stable secondary minerals. The precipitation of secondary minerals is significant for the formation of soil. For example, feldspar, one of the most abundant rock-forming minerals, chemically reacts with water and water-soluble compounds to form clay, such as halloysite and kaolinite[118,119]. In this case, the principal components of the primary mineral (feldspar) (Al and Si) are inherited by the secondary minerals (halloysite and kaolinite).

The trace elements, such as the rare earth elements (REEs), might be enriched or depleted in the altered products depending on the soil and groundwater pH[120]. In South China, the REEs adsorbed on the secondary clay minerals develop world-class heavy rare earth element (HREE) deposits, known as regolith-hosted HREE deposits or ion-adsorption REE deposits, which provide most of the HREE produced in the world[121,122]. Another interesting example is the fate of trace arsenic (As) during the dissolution of As-containing pyrite; As might be adsorbed by the secondary goethite or might be incorporated into the secondary jarosite via substitution for sulfate[123]. Therefore, the minor/trace elements in minerals are hard to form independent secondary minerals during dissolution/weathering. During the dissolution of $(Pb_xCa_{1-x})_5(PO_4)_3OH$ in a laboratory, both $PbHPO_4$ and $Pb_3(PO_4)_2$ formed as secondary products when the Pb molar fraction in the solid solution was high enough ($x \geq 0.3$)[124].

During the dissolution of calcite, the precipitation of several secondary minerals has been observed in the presence of aqueous cations (Pb^{2+}, Cu^{2+}, and UO_2^{2+})[125–128], oxyanions (PO_4^{3-}, AsO_4^{3-}, SbO_4^{3-} and SeO_3^{3-})[129,130], and F^-[131] due to the formation of less soluble phases. Sometimes, calcite might be entirely replaced by the secondary minerals, such as cerussite ($PbCO_3$)[132], dolomite ($CaMg(CO_3)_2$)[133–135], magnesite ($MgCO_3$)[134], siderite ($FeCO_3$)[133], gypsum ($CaSO_4$)[136,137], whewellite ($CaC_2O_4{\cdot}H_2O$)[138] and fluorite (CaF_2)[139,140], via a coupled dissolution–precipitation mechanism. Interestingly, the capture of aqueous Mg on the calcite surface was recognized when calcite dissolved in seawater, resulting in an enriched Mg surface[141]. With the growth of the secondary minerals covering the calcite surface, the dissolution of calcite was inhibited accordingly. Note that almost half of the components of these secondary minerals are liquid sources, which combine with dissolved calcium or carbonate from calcite.

Recently, hydrated Mg-carbonate phases have been identified as the secondary precipitates that form during the dissolution of dolomite and magnesite in pure water[130]. For siderite dissolution, the Raman spectra proved the precipitation of iron oxyhydroxide (goethite or ferrihydrite)[130,142]. When siderite dissolved under extreme conditions, a complex assemblage of Fe^{II}–Fe^{III}-iron oxides forms, which was dominated by wüstite (FeO) but also contained some iron(III) observed as hematite and possibly magnetite or defective wüstite[143]. Except for the hydroxyl group (OH^-), which is the water source, the other elements of these secondary minerals came from the parent dolomite and magnesite. Similarly, the secondary minerals in our experiment, i.e., Ca-poor smithsonite, U-rich calcite, and Co-poor aragonite, inherited all the components of the original impurity-bearing calcite. A possible pathway for the formation of Ca-poor smithsonite and U-rich calcite could be expressed as Eqs. (1) and (2). The dissolved Zn/Ca molar ratio of Zn-calcite was much less than that of the solids, suggesting that more Ca^{2+} was released than Zn^{2+} (Fig. S7). This phenomenon was consistent with Eq. (1). In contrast, the dissolved U/Ca molar ratio was higher than that in the solid, indicating that more UO_2^{2+} ions were released, which provided the possibility of Eq. (2).

$$\mathrm{Ca}_{(1-x)}\mathrm{Zn}_x\mathrm{CO}_{3(s)}(\mathrm{Calcite}) \rightleftharpoons \mathrm{Zn}_y\mathrm{Ca}_z(\mathrm{CO}_3)_{(y+z)(s)}\left(\mathrm{Ca}\ -\ \mathrm{poor}\ \ \mathrm{Smithsonite}\right) + (1-x-z)\mathrm{Ca}^{2+}_{(aq)} + (x-y)\mathrm{Zn}^{2+}_{(aq)} + (1-y-z)\mathrm{CO}^{2-}_{3(aq)} \quad \left(x > y, y > z, \frac{y}{z} > \frac{x}{1-x}\right) \tag{1}$$

$$\mathrm{Ca}_{(1-x)}(\mathrm{UO}_2)_x\mathrm{CO}_{3(s)}(\mathrm{Calcite}) \rightleftharpoons \mathrm{Ca}_y(\mathrm{UO}_2)_z(\mathrm{CO}_3)_{(y+z)(s)}(\mathrm{U}\ -\ \mathrm{rich\ Calcite}) + (1-x-y)\mathrm{Ca}^{2+}_{(aq)} + (x-z)(\mathrm{UO}_2)^{2+}_{(aq)} + (1-y-z)\mathrm{CO}^{2-}_{3(aq)} \quad \left(x > z, y > z, \frac{z}{y} > \frac{x}{1-x}\right) \tag{2}$$

As a typical and well known polymorphic transition, the hydrothermal transformation of aragonite to calcite provides a perfect example of interface-coupled dissolution-reprecipitation[144]. The reverse transformation of calcite to aragonite is also relatively common in nature[145], though it is usually simulated in the laboratory under high-temperature/high-pressure conditions[146–148]. Remarkably, Huang et al. observed the complete transition of high Mg-calcite contents to low Mg-aragonite contents at room temperature/pressure within days[149]. Probably, the formation of Co-poor aragonite in our experiment occurs by a similar mechanism because aragonite is the most stable polymorph of calcium carbonate in the presence of a significant amount of Co^{2+} ions. As mentioned previously, the dissolved Co^{2+} content gradually increased with increasing the dissolution time, and the final released Co^{2+} content observed for Co-08 was as high as 16.13 μM after 2880 h (Fig. 2f). Meanwhile, Co-poor aragonite precipitated as a secondary mineral via the dissolution–precipitation process (Figs. 4e,f, S10a–h). The proposed mechanism is shown in Eq. (3). However, there is no direct evidence at present, thus requiring further study.

$$\mathrm{Ca}_{(1-x)}\mathrm{Co}_x\mathrm{CO}_{3(s)}(\mathrm{Calcite}) \rightleftharpoons \mathrm{Ca}_y\mathrm{Co}_z(\mathrm{CO}_3)_{(y+z)(s)}\left(\mathrm{Co\text{ - }poor\ Aragonite}\right) + \left(1-x-y\right)\mathrm{Ca}^{2+}_{(aq)} + (x-z)\mathrm{Co}^{2+}_{(aq)} + \left(1-y-z\right)\mathrm{CO}^{2-}_{3(aq)} \quad \left(x>z, y>z, \frac{z}{y}<\frac{x}{1-x}\right) \tag{3}$$

Implication to the environment. Calcite occurs in rocks[1,2], soils[150], airborne dust[151,152], organisms[153], and even the human body[154,155] and precipitates as abiogenic and biogenic minerals. In contaminated soils and sediments, bioavailable carbonate-bounded HMs mainly coprecipitate with calcite[156,157]. Moreover, primary carbonate dissolution and secondary carbonate precipitation often happen in soil[158]. Therefore, our results provided further evidence that calcite could control the migration of HMs, especially for Cd, Zn, and Ni. The residual calcite has a higher HM concentration than the primary calcite, which could contribute to the enrichment of Cd and Zn in the soil weathered from limestone[31–34,117]. However, calcite-bound U tends to release during dissolution, suggesting that U might be more sensitive than other metals to soil and ocean acidification. Although the general content of U in natural calcite is 0.1–10 mg/kg and occasionally up to 360 mg/kg[84], the dissolution of limestone could rein in the uranium concentrations in river water[29]. Meanwhile, the change in the calcite solubility indicates that the stability of a carbon sink in soil and ocean might be reconsidered once HMs were incorporated. Last but not least, the precipitation of smithsonite, Co-poor aragonite, U-rich calcite, and the previously reported rhodochrosite ($MnCO_3$) and malachite ($Cu_2(OH)_2CO_3$) indicated a new mineralization pathway of these minerals, i.e., secondary minerals formed after the dissolution of minerals doped with impurity metals.

Conclusion

In this study, four divalent heavy metal (Cd^{2+}, Co^{2+}, Ni^{2+}, and Zn^{2+}) and uranyl (UO_2^{2+})-containing calcite were successfully synthesized with changing the M/Ca molar ratio from 0.05 to 12.36%. With the incorporation of impurities, the calcite crystal sizes decreased with increasing the BET surface area. According to the batch dissolution data, the BET surface area calibrated dissolution rates at the early stage decreased with the increase in the impurity molar fraction, indicating an inhibition effect on the dissolution rate. However, both inhibition and promotion effects were observed on the calcite solubility, depending on the type of impurities and their content. The dissolution of impure calcite is incongruent, especially for Cd-, Ni-, and U-containing calcite. The retention ability of Cd and Ni in calcite is remarkably better than that of U, suggesting the potential risk of uranium release due to U-rich calcite dissolution. Meanwhile, the HRTEM and SAED results demonstrated that partial zinc and uranium were immobilized in the reprecipitated phase as smithsonite and U-rich calcite, respectively. Furthermore, the discovery of Co-poor aragonite as a secondary mineral during the dissolution of Co-calcite provided a new type of calcite-aragonite transition. In conclusion, our results demonstrated that the dissolution process of calcite could be significantly changed by incorporating divalent heavy metals and uranyl cations, which has potential environment and climate implications.

Methods

Solid preparation and characterization. The coprecipitation method followed the method used by our previous investigation[45] and was similar to the method used by Katsikopoulos et al.[66]. First, a 0.1 mol/L heavy metal and uranyl solution (M = Cd^{2+}, Co^{2+}, Ni^{2+}, Zn^{2+}, UO_2^{2+}) and a 1 mol/L $CaCl_2$ solution were mixed with different molar ratios (Table 1). Afterward, a Na_2CO_3 solution was delivered at a constant rate using a peristaltic pump under continuously stirring. The solid-solution precipitates were allowed to age and incubate for three days, and then, the solutions were centrifuged and dried at 80 °C. All the experiments were performed at room temperature and atmospheric pressure. In the following text, the calcite doped with impurities will be recorded as HM-calcite, e.g., Cd-calcite means calcite containing Cd.

The mineral identity of the precipitates was confirmed by X-ray powder diffraction (XRD) using a Bruker D8 Advance powder diffractometer with Ni-filtered Cu–Kα radiation (λ = 1.5406 Å, 40 kV and 40 mA). The samples were scanned from 10° to 80° (2θ), a range that covers the characteristic peaks of calcium carbonate, using a step size of 0.01° (2θ) and a scan rate of 3.0° (2θ) per minute. Then, 0.05 g of each precipitate was dissolved in concentrated HNO_3 and used to analyze the cation contents, which were determined by inductively coupled plasma-optical emission spectrometry (ICP-OES) (VARIAN VISTA PRO) after dilution. The Brunauer–Emmett–Teller (BET) surface area of the precipitates was determined using a Micromeritics ASAP 2020 M surface area analyzer, in which the samples were dried and degassed at room temperature for 24 h using N_2 gas. Scanning electron microscopy (SEM) (ZEISS Gemini 500) was performed to obtain images of the precipitates and to provide an approximate size and morphology of the crystalline samples.

Dissolution experiments and characterization. The procedure of dissolution experiment is the same as described in our previous investigation[45]. In brief, an initial dissolving solution (pH = 5.00 ± 0.05) was prepared using deionized water (18.2 MΩ·cm) and hydrochloric acid (AR). Each 0.125 g of calcite powder was put into a 15 mL polypropylene tube containing 10 mL of the initial reaction solution. Afterward, all the tubes were capped and shaken using an overhead shaker in an incubator chamber at 25 °C. At a specified time, the reaction solution was sampled and filtered by a 0.22 μm pore filter and stored in a clean polyethylene tube. The aqueous pH was measured immediately using a pH meter (Sartorius PB-10). Cations were analyzed using ICP-OES, and the dissolved inorganic carbon (DIC) was measured using a total organic carbon (TOC) analyzer (TOC–VCPH, Shimadzu, Japan). All the dissolution experiments were run in duplicate, and an average was obtained for each metal concentration. Meanwhile, the solids were sampled from the bottles, dried, and preserved for characteri-

zation. The morphology of calcite after dissolution was observed by SEM and a high-resolution transmission electron microscopy (HRTEM) system operated at 200 kV (FEI Talos F200S).

Calculation of solubility and chemical species. The dissolution of pure calcite and impurity-containing calcite can be expressed as Eqs. (4) and (5).

$$CaCO_3 \rightleftharpoons Ca^{2+} + CO_3^{2-} \tag{4}$$

$$Ca_{(1-x)}M_xCO_3 \rightleftharpoons (1-x)Ca^{2+} + xM^{2+} + CO_3^{2-} \tag{5}$$

where x is the molar fraction of MCO_3 in the solid-solution.

The solubility was calculated using the dissolved metal (Ca + M) and stoichiometric carbonate.

The corresponding equilibrium solubility product expression is showing as Eqs. (6) and (7).

$$K_{sp(calcite)} = \left[Ca^{2+}\right] \bullet [CO_3^{2-}] \tag{6}$$

$$K_{sp(impurecalcite)} = \left[Ca^{2+}\right]^{1-x} \bullet \left[M^{2+}\right]^{x} \bullet [CO_3^{2-}] \tag{7}$$

Usually, the ion activity product (IAP) is also used to describe the solubility of a solid[41], as shown in Eqs. (8) and (9).

$$IAP_{(calcite)} = \alpha_{Ca^{2+}} \bullet \alpha_{CO_3^{2-}} \tag{8}$$

$$IAP_{(impure\ calcite)} = \left(\alpha_{Ca^{2+}}\right)^{1-x} \cdot \left(\alpha_{M^{2+}}\right)^{x} \cdot \left(\alpha_{CO_3^{2-}}\right) \tag{9}$$

where α_i is the activity of species i.

However, Davis et al. used the same IAP expression for Mg-calcite that was used for pure calcite[44].

In this investigation, the species activity and saturation index (Table S1) were calculated using Visual MINTEQ. For comparison, IAP was expressed in the same way as it was expressed by Davis et al.[44].

Data availability

The datasets generated during and/or analyzed during the current study, whether they were included in this published article and its Supplementary Information files or not, are available from the corresponding author upon reasonable request.

Received: 22 May 2020; Accepted: 16 September 2020
Published online: 08 October 2020

References

1. Chang, L. L. Y. Carbonates. *In Non-silicates: Sulphates, carbonates, phosphates, halides* 5**B**, 95–288 (The Geological Society, New York, 1998).
2. Hazen, R. M., Downs, R. T., Jones, A. P. & Kah, L. Carbon mineralogy and crystal chemistry. *Rev. Miner. Geochem.* **75**, 7–46 (2013).
3. Martin, J. B. Carbonate minerals in the global carbon cycle. *Chem. Geol.* **449**, 58–72 (2017).
4. Curti, E. Coprecipitation of radionuclides with calcite: estimation of partition coefficients based on a review of laboratory investigations and geochemical data. *Appl. Geochem.* **14**, 433–445 (1999).
5. Stipp, S. L. S., Christensen, J. T., Lakshtanov, L. Z., Baker, J. A. & Waight, T. E. Rare earth element (REE) incorporation in natural calcite: upper limits for actinide uptake in a secondary phase. *Radiochim. Acta* **94**, 523–528 (2006).
6. Olsson, J., Stipp, S. L. S., Makovicky, E. & Gislason, S. R. Metal scavenging by calcium carbonate at the Eyjafjallajökull volcano: a carbon capture and storage analogue. *Chem. Geol.* **384**, 135–148 (2014).
7. Drake, H. *et al.* Incorporation of metals into calcite in a deep anoxic granite aquifer. *Environ. Sci. Technol.* **52**, 493–502 (2018).
8. Chi, J., Zhang, W., Wang, L. & Putnis, C. V. Direct observations of the occlusion of soil organic matter within calcite. *Environ. Sci. Technol.* **53**, 8097–8104 (2019).
9. Ware, J. R., Smith, S. V. & Reaka-Kudla, M. L. Coral reefs: sources or sinks of atmospheric CO_2?. *Coral Reefs* **11**, 127–130 (1992).
10. Kelemen, P. B. & Matter, J. In situ carbonation of peridotite for CO_2 storage. *Proc. Natl. Acad. Sci. USA* **105**, 17295–17300 (2008).
11. Kunhikrishnan, A. *et al.* Functional relationships of soil acidification, liming, and greenhouse gas flux. *Adv. Agron.* **139**, 1–71 (2016).
12. Holland, J. E. *et al.* Liming impacts on soils, crops and biodiversity in the UK: a review. *Sci. Total Environ.* **610–611**, 316–332 (2018).
13. McBride, M. B. *Reactions controlling heavy metal solubility in soils. Advances in Soil Science* 10th edn. (Springer, New York, 1989).
14. Lee, S. H., Lee, J. S., Jeong Choi, Y. & Kim, J. G. In situ stabilization of cadmium-, lead-, and zinc-contaminated soil using various amendments. *Chemosphere* **77**, 1069–1075 (2009).
15. Phillips, A. J. *et al.* Engineered applications of ureolytic biomineralization: a review. *Biofouling* **29**, 715–733 (2013).
16. Kumari, D. *et al.* Microbially-induced carbonate precipitation for immobilization of toxic metals. *Adv. Appl. Microbiol.* **94**, 79–108 (2016).
17. Gat, D., Ronen, Z. & Tsesarsky, M. Long-term sustainability of microbial-induced $CaCO_3$ precipitation in aqueous media. *Chemosphere* **184**, 524–531 (2017).
18. Guo, J. H. *et al.* Significant acidification in major chinese croplands. *Science* **327**, 1008–1010 (2010).
19. Rice, K. C. & Herman, J. S. Acidification of earth: an assessment across mechanisms and scales. *Appl. Geochem.* **27**, 1–14 (2012).
20. Doney, S. C., Fabry, V. J., Feely, R. A. & Kleypas, J. A. Ocean acidification: the other CO_2 problem. *Ann. Rev. Mar. Sci.* **1**, 169–192 (2009).
21. Feely, R. A. *et al.* Impact of anthropogenic CO_2 on the $CaCO_3$ system in the oceans. *Science* **305**, 362–366 (2004).

22. Orr, J. C. *et al.* Anthropogenic ocean acidification over the twenty-first century and its impact on calcifying organisms. *Nature* **437**, 681–686 (2005).
23. Hoegh-Guldberg, O. *et al.* Coral reefs under rapid climate change and ocean acidification. *Science* **318**, 1737–1742 (2007).
24. Sulpis, O. *et al.* Current $CaCO_3$ dissolution at the seafloor caused by anthropogenic CO_2. *Proc. Natl. Acad. Sci. USA.* **115**, 11700–11705 (2018).
25. Kopáček, J. *et al.* Climate change increasing calcium and magnesium leaching from granitic alpine catchments. *Environ. Sci. Technol.* **51**, 159–166 (2017).
26. Weyhenmeyer, G. A. *et al.* Widespread diminishing anthropogenic effects on calcium in freshwaters. *Sci. Rep.* **9**, 1–10 (2019).
27. Kirsch, K., Navarre-Sitchler, A. K., Wunsch, A. & McCray, J. E. Metal release from sandstones under experimentally and numerically simulated CO_2 leakage conditions. *Environ. Sci. Technol.* **48**, 1436–1442 (2014).
28. Wunsch, A., Navarre-Sitchler, A. K., Moore, J. & McCray, J. E. Metal release from limestones at high partial-pressures of CO_2. *Chem. Geol.* **363**, 40–55 (2014).
29. Palmer, M. R. & Edmond, J. M. Uranium in river water. *Geochim. Cosmochim. Acta* **57**, 4947–4955 (1993).
30. Edmond, J. M. Himalayan tectonics, weathering processes, and the strontium isotope record in marine limestones. *Science* **258**, 1594–1597 (1992).
31. Quezada-Hinojosa, R. P., Matera, V., Adatte, T., Rambeau, C. & Föllmi, K. B. Cadmium distribution in soils covering Jurassic oolitic limestone with high Cd contents in the Swiss Jura. *Geoderma* **150**, 287–301 (2009).
32. Rambeau, C. M. C. *et al.* High cadmium concentrations in Jurassic limestone as the cause for elevated cadmium levels in deriving soils: a case study in Lower Burgundy, France. *Environ. Earth Sci.* **61**, 1573–1585 (2010).
33. Wen, Y., Li, W., Yang, Z., Zhang, Q. & Ji, J. Enrichment and source identification of Cd and other heavy metals in soils with high geochemical background in the karst region, Southwestern China. *Chemosphere* **245**, 125620 (2020).
34. Qu, S., Wu, W., Nel, W. & Ji, J. The behavior of metals/metalloids during natural weathering: a systematic study of the monolithological watersheds in the upper Pearl River Basin, China. *Sci. Total Environ.* **708**, 134572 (2020).
35. Xia, X. *et al.* Cadmium risk in the soil-plant system caused by weathering of carbonate bedrock. *Chemosphere* **254**, 126799 (2020).
36. Morse, J. W. The kinetics of calcium carbonate dissolution and precipitation in carbonates: mineralogy and chemistry. *Rev. Miner. Geochem.* **11**, 191–225 (1983).
37. Morse, J. W. & Arvidson, R. S. The dissolution kinetics of major sedimentary carbonate minerals. *Earth Sci. Rev.* **58**, 51–84 (2002).
38. Morse, J. W., Arvidson, R. S. & Lüttge, A. Calcium carbonate formation and dissolution. *Chem. Rev.* **107**, 342–381 (2007).
39. Arvidson, R. S. *et al.* Magnesium inhibition of calcite dissolution kinetics. *Geochim. Cosmochim. Acta* **70**, 583–594 (2006).
40. Harstad, A. O. & Stipp, S. L. S. Calcite dissolution: Effects of trace cations naturally present in Iceland spar calcites. *Geochim. Cosmochim. Acta* **71**, 56–70 (2007).
41. Mackenzie, F. T. *et al.* Magnesian calcites: low-temperature occurrence, solubility and solid-solution behavior in carbonates: mineralogy and chemistry. *Rev. Miner. Geochem.* **11**, 97–144 (1983).
42. Bischoff, W. D., Mackenzie, F. T. & Bishop, F. C. Stabilities of synthetic magnesian calcites in aqueous solution: comparison with biogenic materials. *Geochim. Cosmochim. Acta* **51**, 1413–1423 (1987).
43. Busenberg, E. & Niel Plummer, L. Thermodynamics of magnesian calcite solid-solutions at 25 °C and 1 atm total pressure. *Geochim. Cosmochim. Acta* **53**, 1189–1208 (1989).
44. Davis, K. J., Dove, P. M. & De Yoreo, J. J. The role of Mg^{2+} as an impurity in calcite growth. *Science* **290**, 1134–1137 (2000).
45. Zhang, X., Wu, S. & Chen, F. Nano precipitates formed during the dissolution of calcite incorporated with Cu and Mn. *Minerals* **8**, 484 (2018).
46. Haese, R. R., Smith, J., Weber, R. & Trafford, J. High-magnesium calcite dissolution in tropical continental shelf sediments controlled by ocean acidification. *Environ. Sci. Technol.* **48**, 8522–8528 (2014).
47. Rauls, M. *et al.* Influence of impurities on crystallization kinetics - a case study on ammonium sulfate. *J. Cryst. Growth* **213**, 116–128 (2000).
48. Latta, D. E., Pearce, C. I., Rosso, K. M., Kemner, K. M. & Boyanov, M. I. Reaction of U^{VI} with titanium-substituted magnetite: influence of Ti on U^{IV} speciation. *Environ. Sci. Technol.* **47**, 4121–4130 (2013).
49. World Data Centre for Greenhouse Gases (WDCGG). https://gaw.kishou.go.jp.
50. RRUFFa. https://rruff.info/repository/sample_child_record_powder/by_minerals/Smithsonite__R040035-1__Powder__DIF_File__3114.txt.
51. RRUFFb. https://rruff.info/repository/sample_child_record_powder/by_minerals/Aragonite__R080142-9__Powder__DIF_File__11841.txt.
52. RRUFFc. https://rruff.info/repository/sample_child_record_powder/by_minerals/Calcite__R050130-1__Powder__DIF_File__4388.txt.
53. Reeder, R. J. Crystal chemistry of the rhombohedral carbonates in carbonates: mineralogy and chemistry. *Rev. Miner. Geochem.* **11**, 1–47 (1983).
54. Chang, L. L. Y. & Brice, W. R. Subsolidus phase relations in the system calcium carbonate-cadmium carbonate. *Am. Miner.* **56**, 338–341 (1971).
55. Lorens, R. B. Sr. Cd, Mn and Co distribution coefficients in calcite as a function of calcite precipitation rate. *Geochim. Cosmochim. Acta* **45**, 553–561 (1981).
56. Stipp, S. L., Hochella, M. F., Parks, G. A. & Leckie, J. O. Cd^{2+} uptake by calcite, solid-state diffusion, and the formation of solid-solution: Interface processes observed with near-surface sensitive techniques (XPS, LEED, and AES). *Geochim. Cosmochim. Acta* **56**, 1941–1954 (1992).
57. Reeder, R. J. Interaction of divalent cobalt, zinc, cadmium, and barium with the calcite surface during layer growth. *Geochim. Cosmochim. Acta* **60**, 1543–1552 (1996).
58. Tesoriero, A. J. & Pankow, J. F. Solid solution partitioning of Sr^{2+}, Ba^{2+}, and Cd^{2+} to calcite. *Geochim. Cosmochim. Acta* **60**, 1053–1063 (1996).
59. Prieto, M., Cubillas, P. & Fernández-Gonzalez, Á. Uptake of dissolved Cd by biogenic and abiogenic aragonite: a comparison with sorption onto calcite. *Geochim. Cosmochim. Acta* **67**, 3859–3869 (2003).
60. Horner, T. J., Rickaby, R. E. M. & Henderson, G. M. Isotopic fractionation of cadmium into calcite. *Earth Planet. Sci. Lett.* **312**, 243–253 (2011).
61. Moureaux, C. *et al.* Effects of field contamination by metals (Cd, Cu, Pb, Zn) on biometry and mechanics of echinoderm ossicles. *Aquat. Toxicol.* **105**, 698–707 (2011).
62. Xu, M. *et al.* Heterogeneous growth of cadmium and cobalt carbonate phases at the (1014) calcite surface. *Chem. Geol.* **397**, 24–36 (2015).
63. Lamble, G. M., Reeder, R. J. & Northrup, P. A. Characterization of heavy metal incorporation in calcite by XAFS spectroscopy. *J. Phys. IV* **7**, 793–797 (1997).
64. Reeder, R. J., Lamble, G. M. & Northrup, P. A. XAFS study of the coordination and local relaxation around Co^{2+}, Zn^{2+}, Pb^{2+} and Ba^{2+} trace elements in calcite. *Am. Miner.* **84**, 1049–1060 (1999).

65. Cheng, L., Sturchio, N. C. & Bedzyk, M. J. Local structure of incorporated at the calcite surface: an X-ray standing wave and SEXAFS study. *Phys. Rev. B Condens. Matter Mater. Phys.* **61**, 4877–4883 (2000).
66. Katsikopoulos, D., Fernández-González, Á, Prieto, A. C. & Prieto, M. Co-crystallization of Co(II) with calcite: implications for the mobility of cobalt in aqueous environments. *Chem. Geol.* **254**, 87–100 (2008).
67. González-López, J. *et al.* Cobalt incorporation in calcite: thermochemistry of (Ca, Co)CO_3 solid solutions from density functional theory simulations. *Geochim. Cosmochim. Acta* **142**, 205–216 (2014).
68. González-López, J., Fernández-González, Á & Jiménez, A. Precipitation behaviour in the system Ca^{2+}-Co^{2+}-CO_3^{2+}-H_2O at ambient conditions: amorphous phases and $CaCO_3$ polymorphs. *Chem. Geol.* **482**, 91–100 (2018).
69. De Giudici, G. *et al.* Coordination environment of Zn in foraminifera Elphidium aculeatum and Quinqueloculina seminula shells from a polluted site. *Chem. Geol.* **477**, 100–111 (2018).
70. Cheng, L. *et al.* High-resolution structural study of zinc ion incorporation at the calcite cleavage surface. *Surf. Sci.* **415**, 976–982 (1998).
71. Elzinga, E. & Reeder, R. X-ray absorption spectroscopy study of Cu^{2+} and Zn^{2+} adsorption complexes at the calcite surface: implications for site-specific metal incorporation preferences during calcite crystal growth. *Geochim. Cosmochim. Acta* **66**, 3943–3954 (2002).
72. Elzinga, E. J., Rouff, A. A. & Reeder, R. J. The long-term fate of Cu^{2+}, Zn^{2+}, and Pb^{2+} adsorption complexes at the calcite surface: an X-ray absorption spectroscopy study. *Geochim. Cosmochim. Acta* **70**, 2715–2725 (2006).
73. Menadakis, M., Maroulis, G. & Koutsoukos, P. G. A quantum chemical study of doped $CaCO_3$ (calcite). *Comput. Mater. Sci.* **38**, 522–525 (2007).
74. Liu, X., Lu, X., Liu, X. & Zhou, H. Atomistic simulation on mixing thermodynamics of calcite-smithsonite solid solutions. *Am. Miner.* **100**, 172–180 (2015).
75. van Dijk, I., de Nooijer, L. J., Wolthers, M. & Reichart, G. J. Impacts of pH and [CO_3^{2-}] on the incorporation of Zn in foraminiferal calcite. *Geochim. Cosmochim. Acta* **197**, 263–277 (2017).
76. Hoffmann, U. & Stipp, S. L. S. The behavior of Ni^{2+} on calcite surfaces. *Geochim. Cosmochim. Acta* **65**, 4131–4139 (2001).
77. Lakshtanov, L. Z. & Stipp, S. L. S. Experimental study of nickel(II) interaction with calcite: adsorption and coprecipitation. *Geochim. Cosmochim. Acta* **71**, 3686–3697 (2007).
78. Munsel, D. et al. Heavy metal incorporation in foraminiferal calcite: results from multi-element enrichment culture experiments with Ammonia tepida. *Biogeosciences* **7**, 2339–2350 (2010).
79. Andersson, M. P., Sakuma, H. & Stipp, S. L. S. Strontium, nickel, cadmium, and lead substitution into calcite, studied by density functional theory. *Langmuir* **30**, 6129–6133 (2014).
80. Reeder, R. J., Nugent, M., Lamble, G. M., Tait, C. D. & Morris, D. E. Uranyl incorporation into calcite and aragonite: XAFS and luminescence studies. *Environ. Sci. Technol.* **34**, 638–644 (2000).
81. Reeder, R. J. et al. Coprecipitation of uranium(VI) with calcite: XAFS, micro-XAS, and luminescence characterization. *Geochim. Cosmochim. Acta* **65**, 3491–3503 (2001).
82. Chen, X., Romaniello, S. J., Herrmann, A. D., Wasylenki, L. E. & Anbar, A. D. Uranium isotope fractionation during coprecipitation with aragonite and calcite. *Geochim. Cosmochim. Acta* **188**, 189–207 (2016).
83. Niu, Z. et al. Spectroscopic studies on U(VI) incorporation into $CaCO_3$: effects of aging time and U(VI) concentration. *Chemosphere* **220**, 1100–1107 (2019).
84. Kelly, S. D. et al. Uranyl incorporation in natural calcite. *Environ. Sci. Technol.* **37**, 1284–1287 (2003).
85. Reeder, R. J. et al. Site-specific incorporation of uranyl carbonate species at the calcite surface. *Geochim. Cosmochim. Acta* **68**, 4799–4808 (2004).
86. Wang, Z., Zachara, J. M., Mckinley, J. P. & Smith, S. C. Cryogenic laser induced U(VI) fluorescence studies of a U(VI) substituted natural calcite: implications to U(VI) speciation in contaminated hanford sediments. *Environ. Sci. Technol.* **39**, 2651–2659 (2005).
87. Kelly, S. D., Rasbury, E. T., Chattopadhyay, S., Kropf, A. J. & Kemner, K. M. Evidence of a stable uranyl site in ancient organic-rich calcite. *Environ. Sci. Technol.* **40**, 2262–2268 (2006).
88. Arai, Y., Marcus, M. A., Tamura, N., Davis, J. A. & Zachara, J. M. Spectroscopic evidence for uranium bearing precipitates in vadose zone sediments at the Hanford 300-area site. *Environ. Sci. Technol.* **41**, 4633–4639 (2007).
89. Keul, N. et al. Incorporation of uranium in benthic foraminiferal calcite reflects seawater carbonate ion concentration. *Geochem. Geophys. Geosyst.* **14**, 102–111 (2013).
90. Balboni, E., Morrison, J. M., Wang, Z., Engelhard, M. H. & Burns, P. C. Incorporation of Np(V) and U(VI) in carbonate and sulfate minerals crystallized from aqueous solution. *Geochim. Cosmochim. Acta* **151**, 133–149 (2015).
91. Smith, K. F. *et al.* U(VI) behaviour in hyperalkaline calcite systems. *Geochim. Cosmochim. Acta* **148**, 343–359 (2015).
92. Walker, S. M. & Becker, U. Uranyl(VI) and neptunyl(V) incorporation in carbonate and sulfate minerals: insight from first-principles. *Geochim. Cosmochim. Acta* **161**, 19–35 (2015).
93. Lee, Y. J., Reeder, R. J., Wenskus, R. W. & Elzinga, E. J. Structural relaxation in the $MnCO_3$–$CaCO_3$ solid solution: a Mn K-edge EXAFS study. *Phys. Chem. Miner.* **29**, 585–594 (2002).
94. Rouff, A. A., Elzinga, E. J., Reeder, R. J. & Fisher, N. S. X-ray absorption spectroscopic evidence for the formation of Pb(II) inner-Sphere adsorption complexes and precipitates at the calcite–water interface. *Environ. Sci. Technol.* **38**, 1700–1707 (2004).
95. Kerisit, S. N. & Prange, M. P. Ab initio molecular dynamics simulation of divalent metal cation incorporation in calcite: implications for interpreting X-ray absorption spectroscopy data. *ACS Earth Spectr. Chem.* **3**, 2582 (2019).
96. Elzinga, E. J. *et al.* EXAFS study of rare-earth element coordination in calcite. *Geochim. Cosmochim. Acta* **66**, 2875–2885 (2002).
97. Heberling, F., Denecke, M. A. & Bosbach, D. Neptunium(V) coprecipitation with calcite. *Environ. Sci. Technol.* **42**, 471–476 (2008).
98. Sturchio, N. C., Antonio, M. R., Soderholm, L., Sutton, S. R. & Brannon, J. C. Tetravalent uranium in calcite. *Science* **281**, 971–973 (1998).
99. Stumpf, T., Marques Fernandes, M., Walther, C., Dardenne, K. & Fanghänel, T. Structural characterization of Am incorporated into calcite: A TRLFS and EXAFS study. *J. Colloid Interface Sci.* **302**, 240–245 (2006).
100. Podder, J. *et al.* Iodate in calcite and vaterite: insights from synchrotron X-ray absorption spectroscopy and first-principles calculations. *Geochim. Cosmochim. Acta* **198**, 218–228 (2017).
101. Saslow, S. A. *et al.* Chromate effect on iodate incorporation into calcite. *ACS Earth Spectr. Chem.* **3**, 1624–1630 (2019).
102. Tang, Y., Elzinga, E. J., Jae Lee, Y. & Reeder, R. J. Coprecipitation of chromate with calcite: batch experiments and X-ray absorption spectroscopy. *Geochim. Cosmochim. Acta* **71**, 1480–1493 (2007).
103. Aurelio, G. et al. Structural study of selenium(IV) substitutions in calcite. *Chem. Geol.* **270**, 249–256 (2010).
104. Bardelli, F. et al. Arsenic uptake by natural calcite: an XAS study. *Geochim. Cosmochim. Acta* **75**, 3011–3023 (2011).
105. Alexandratos, V. G., Elzinga, E. J. & Reeder, R. J. Arsenate uptake by calcite: macroscopic and spectroscopic characterization of adsorption and incorporation mechanisms. *Geochim. Cosmochim. Acta* **71**, 4172–4187 (2007).
106. Füger, A., Konrad, F., Leis, A., Dietzel, M. & Mavromatis, V. Effect of growth rate and pH on lithium incorporation in calcite. *Geochim. Cosmochim. Acta* **248**, 14–24 (2019).
107. vander Putten, E., Dehairs, F., Keppens, E. & Baeyens, W. High resolution distribution of trace elements in the calcite shell layer of modern Mytilus edulis: environmental and biological controls. *Geochim. Cosmochim. Acta* **64**, 997–1011 (2000).
108. Vielzeuf, D. *et al.* Distribution of sulphur and magnesium in the red coral. *Chem. Geol.* 355, 13–27 (2013).

109. Trong Nguyen, L. *et al*. Distribution of trace element in Japanese red coral Paracorallium japonicum by μ-XRF and sulfur speciation by XANES: linkage between trace element distribution and growth ring formation. *Geochim. Cosmochim. Acta* **127**, 1–9 (2014).
110. Tanaka, K. *et a*l. Microscale magnesium distribution in shell of the Mediterranean mussel Mytilus galloprovincialis: an example of multiple factors controlling Mg/Ca in biogenic calcite. *Chem. Geol.* **511**, 521–532 (2019).
111. Drake, H., Tullborg, E. L., Hogmalm, K. J. & Åström, M. E. Trace metal distribution and isotope variations in low-temperature calcite and groundwater in granitoid fractures down to 1km depth. *Geochim. Cosmochim. Acta* **84**, 217–238 (2012).
112. Gabitov, R. I., Sadekov, A. & Migdisov, A. REE incorporation into calcite individual crystals as one time spike addition. *Minerals* **7**, 1–11 (2017).
113. Svensson, U. & Dreybrodt, W. Dissolution kinetics of natural calcite minerals in CO_2-water systems approaching calcite equilibrium. *Chem. Geol.* **100**, 129–145 (1992).
114. Eisenlohr, L., Meteva, K., Gabrovšek, F. & Dreybrodt, W. The inhibiting action of intrinsic impurities in natural calcium carbonate minerals to their dissolution kinetics in aqueous H_2O–CO_2 solutions. *Geochim. Cosmochim. Acta* **63**, 989–1001 (1999).
115. Briese, L., Arvidson, R. S. & Luttge, A. The effect of crystal size variation on the rate of dissolution: a kinetic Monte Carlo study. *Geochim. Cosmochim. Acta* **212**, 167–175 (2017).
116. Noiriel, C., Oursin, M. & Daval, D. Examination of crystal dissolution in 3D: a way to reconcile dissolution rates in the laboratory? *Geochim. Cosmochim. Acta* **273**, 1–25 (2020).
117. Jacquat, O., Voegelin, A., Juillot, F. & Kretzschmar, R. Changes in Zn speciation during soil formation from Zn-rich limestones. *Geochim. Cosmochim. Acta* **73**, 5554–5571 (2009).
118. Wilson, M. J. Weathering of the primary rock-forming minerals: processes, products and rates. *Clay Miner*. **39**, 233–266 (2004).
119. Velde, B. & Alain, M. *The Origin of Clay Minerals in Soils and Weathered Rocks* (Springer, New York, 2008).
120. Nesbitt, H. W. Mobility and fractionation of rare earth elements during weathering of a granodiorite. *Nature* **279**, 206–210 (1979).
121. Li, M. Y. H., Zhou, M. F. & Williams-Jones, A. E. The genesis of regolith-hosted heavy rare earth element deposits: insights from the world-class Zudong deposit in Jiangxi province, South China. *Econ. Geol.* **114**, 541–568 (2019).
122. Li, M. Y. H. & Zhou, M. F. The role of clay minerals in formation of the regolith-hosted heavy rare earth element deposits. *Am. Miner.* **105**, 92–108 (2020).
123. Savage, K. S., Tingle, T. N., O'Day, P. A., Waychunas, G. A. & Bird, D. K. Arsenic speciation in pyrite and secondary weathering phases, Mother Lode Gold District, Tuolumne County, California. *Appl. Geochem*. **15**, 1219–1244 (2000).
124. Zhu, Y. *et al*. Characterization, dissolution and solubility of the hydroxypyromorphite-hydroxyapatite solid solution $[(Pb_xCa_{1-x})5(PO_4)_3OH]$ at 25 °C and pH 2–9. *Geochem. Trans.* **17**, 1–18 (2016).
125. Godelitsas, A., Astilleros, J. M., Hallam, K., Harissopoulos, S. & Putnis, A. Interaction of calcium carbonates with lead in aqueous solutions. *Environ. Sci. Technol*. **37**, 3351–3360 (2003).
126. Schindler, M., Hawthorne, F. C., Putnis, C. & Putnis, A. Growth of uranyl-hydroxy-hydrate and uranyl-carbonate minerals on the (104) surface of calcite. Can. *Mineral.* **42**, 1683–1697 (2004).
127. Schindler, M. & Putnis, A. Crystal growth of schoepite on the (104) surface of calcite. Can. *Mineral*. **42**, 1667–1681 (2004).
128. Tang, H., Xian, H., He, H., Wei, J. & Liu, H. Science of the total environment kinetics and mechanisms of the interaction between the calcite (10.4) surface and Cu^{2+}-bearing solutions. *Sci. Total Environ*. **668**, 602–616 (2019).
129. Klasa, J. *et al*. An atomic force microscopy study of the dissolution of calcite in the presence of phosphate ions. *Geochim. Cosmochim. Acta* **117**, 115–128 (2013).
130. Renard, F., Røyne, A. & Putnis, C. V. Timescales of interface-coupled dissolution-precipitation reactions on carbonates. *Geosci. Front*. **10**, 17–27 (2019).
131. Yang, T., Huh, W., Jho, J. Y. & Kim, I. W. Effects of fluoride and polymeric additives on the dissolution of calcite and the subsequent formation of fluorite. *Colloids Surf. A* **451**, 75–84 (2014).
132. Yuan, K., Lee, S. S., De Andrade, V., Sturchio, N. C. & Fenter, P. Replacement of calcite ($CaCO_3$) by cerussite (PbCO3). *Environ. Sci. Technol*. **50**, 12984–12991 (2016).
133. Pearce, M. A., Timms, N. E., Hough, R. M. & Cleverley, J. S. Reaction mechanism for the replacement of calcite by dolomite and siderite: implications for geochemistry, microstructure and porosity evolution during hydrothermal mineralisation. *Contrib. Miner. Pet*. **166**, 995–1009 (2013).
134. Jonas, L., Müller, T., Dohmen, R., Baumgartner, L. & Putlitz, B. Transport-controlled hydrothermal replacement of calcite by Mg-carbonates. *Geology* **43**, 779–783 (2015).
135. Kondratiuk, P., Tredak, H., Ladd, A. J. C. & Szymczak, P. Synchronization of dissolution and precipitation fronts during infiltration-driven replacement in porous rocks. *Geophys. Res. Lett.* **42**, 2244–2252 (2015).
136. Takahashi, Y., Miyoshi, T., Yabuki, S., Inada, Y. & Shimizu, H. Observation of transformation of calcite to gypsum in mineral aerosols by Ca K-edge X-ray absorption near-edge structure (XANES). *Atmos. Environ*. **42**, 6535–6541 (2008).
137. Ruiz-Agudo, E. *et al*. Experimental study of the replacement of calcite by calcium sulphates. *Geochim. Cosmochim. Acta* **156**, 75–93 (2015).
138. Ruiz-Agudo, E., Álvarez-Lloret, P., Putnis, C. V., Rodriguez-Navarro, A. B. & Putnis, A. Influence of chemical and structural factors on the calcite-calcium oxalate transformation. *CrystEngComm* **15**, 9968–9979 (2013).
139. Pedrosa, E. T., Boeck, L., Putnis, C. V. & Putnis, A. The replacement of a carbonate rock by fluorite: kinetics and microstructure. *Am. Miner.* **102**, 126–134 (2017).
140. Glover, E. D. & Sippel, R. F. Experimental pseudomorphs: replacement of calcite by fluorite. *Am. Miner*. **47**, 1156–1165 (1962).
141. Subhas, A. V. *et al*. Catalysis and chemical mechanisms of calcite dissolution in seawater. *Proc. Natl. Acad. Sci. USA* **114**, 8175–8180 (2017).
142. Renard, F., Putnis, C. V., Montes-Hernandez, G. & King, H. E. Siderite dissolution coupled to iron oxyhydroxide precipitation in the presence of arsenic revealed by nanoscale imaging. *Chem. Geol*. **449**, 123–134 (2017).
143. Marocchi, M., Bureau, H., Fiquet, G. & Guyot, F. In-situ monitoring of the formation of carbon compounds during the dissolution of iron(II) carbonate (siderite). *Chem. Geol*. **290**, 145–155 (2011).
144. Perdikouri, C., Piazolo, S., Kasioptas, A., Schmidt, B. C. & Putnis, A. Hydrothermal replacement of aragonite by calcite: interplay between replacement, fracturing and growth. *Eur. J. Miner*. **25**, 123–136 (2013).
145. Greer, H. F., Zhou, W. & Guo, L. Phase transformation of Mg-calcite to aragonite in active-forming hot spring travertines. *Miner. Pet.* **109**, 453–462 (2015).
146. Hacker, B. R., Kirby, S. H. & Bohlen, S. R. Time and metamorphic petrology: calcite to aragonite experiments. *Science* **258**, 110–112 (1992).
147. Hacker, B. R., Rubie, D. C., Kirby, S. H. & Bohlen, S. R. The calcite → aragonite transformation in low-Mg marble: equilibrium relations, transformations mechanisms, and rates. *J. Geophys. Res. Solid Earth* **110**, 1–16 (2005).
148. Lin, S. J. & Huang, W. L. Polycrystalline calcite to aragonite transformation kinetics: experiments in synthetic systems. *Contrib. Miner. Pet.* **147**, 604–614 (2004).
149. Huang, Y. C. *et al*. Calcium-43 NMR studies of polymorphic transition of calcite to aragonite. *J. Phys. Chem. B* **116**, 14295–14301 (2012).
150. Monger, H. C., Daugherty, L. A. & Lindemann, W. C. Microbial precipitation of pedogenic calcite. *Geology* **19**, 997–1000 (1991).

151. Claquin, T., Schulz, M. & Balkanski, Y. J. Modeling the mineralogy of atmospheric dust sources. *J. Geophys. Res. Atmos.* **104**, 22243–22256 (1999).
152. Engelbrecht, J. P. & Derbyshire, E. Airborne mineral dust. *Elements* **6**, 241–246 (2010).
153. Falini, G., Albeck, S., Weiner, S. & Addadi, L. Control of aragonite or calcite polymorphism by mollusk shell macromolecules. *Science* **271**, 67–69 (1996).
154. Rodgers, A. L. & Spector, M. Human stones. *Endeavour* **5**, 119–126 (1981).
155. Baconnier, S. *et al*. Calcite microcrystals in the pineal gland of the human brain: first physical and chemical studies. *Bioelectromagnetics* **23**, 488–495 (2002).
156. Tessier, A., Campbell, P. G. C. & Bisson, M. Sequential extraction procedure for the speciation of particulate trace metals. *Anal. Chem*. **51**, 844–851 (1979).
157. Gleyzes, C., Tellier, S. & Astruc, M. Fractionation studies of trace elements in contaminated soils and sediments: a review of sequential extraction procedures. *Trends Anal. Chem*. **21**, 451–467 (2002).
158. Bronick, C. J. & Lal, R. Soil structure and management: a review. *Geoderma* **124**, 3–22 (2005).

Acknowledgements

We are grateful for the financial support provided by the National Natural Science Foundation of China (Grant No. 41877135), Natural Science Foundation of Guangdong Province (Grant No. 2017A030313223), Science and Technology Program of Guangzhou, China (Grant No. 201804020037), the Science and Technology Planning Project of Guangdong Province (Grant Nos. 2017B020236003 and 2020B1212060055) and the One-Three-Five Program of Guangzhou Institute of Geochemistry, Chinese Academy of Sciences (GIGCAS) (Grant No. 135PY201604). S. Wu would like to thank the Tuguangchi Award for Excellent Young Scholar GIGCAS. This is contribution No. IS-2910 from GIGCAS.

Author contributions

S.W. developed the concept. X.Z. synthesized the samples and undertook the dissolution experiment and most of the characterization; X.Z. and J.G. performed the XRD, SEM, and TEM characterizations; X.Z. and S.W. analyzed the data and wrote the paper. All authors were involved in multiple revisions of the text and figures.

Competing interests

The authors declare no competing interests.

Additional information

Supplementary information is available for this paper at https://doi.org/10.1038/s41598-020-73555-6.

Correspondence and requests for materials should be addressed to S.W.

Reprints and permissions information is available at www.nature.com/reprints.

Publisher's note Springer Nature remains neutral with regard to jurisdictional claims in published maps and institutional affiliations.